CHAPTER 12: PLASMA INTERFACE ISSUES AND EDGE MODELING

Contributors

Lead Author: T.D. Rognlien

12.1 Introduction (T.D. Rognlien)

12.2 Edge Profiles of the Hydrogenic Plasma (T.D. Rognlien and M.E. Rensink)

12.3 Impurities from First-Wall Evaporation (T.D Rognlien and M.E. Rensink)

12.4 Impurities from High Heat-Load Divertor Regions (J.N. Brooks)

12.5 Large Transient Heat Hoads - Disruptions (A. Hassanein)

12.6 Impact of Edge Conditions on Core Performance (T.E. Evans, C. Wong)

12.7 Modeling Experimental Test Facilities (T.E. Evans, R. Maingi)

12. PLASMA INTERFACE ISSUES AND EDGE MODELING

12.1 Introduction

The edge plasma provides the interface between the hot core plasma and the liquid first-walls and divertor plates. The liquid surfaces can impact the edge and core plasmas by releasing impurities through sputtering, recycling, and evaporation. Such impurities degrade fusion core performance through enhanced radiation loss and fuel dilution. The tolerable levels of core impurity concentration owing to radiative energy loss [1] and to fuel dilution are shown in Fig. 12.1-1 for a tokamak. Changes in the edge plasma temperature and gradient scale-lengths can also affect the stability of the core-edge plasma, *e.g.*, the L-H transition, ELMs, and disruptions. The edge plasma, in turn, influences the liquid surfaces through particle bombardment and line radiation from excited ions. The bombardment leads to sputtering and recycling, and both bombardment and radiation heat the surface that results in increased evaporation. The maximum tolerable evaporation rate specifies the maximum surface temperature of the liquid and sputtering specifies the allowable edge-plasma energy flux and spectrum incident on the wall. While the APEX project has primarily focused on studying the performance of the entire first-wall, the response of liquid divertor plates for tokamaks (studied under the ALPS project) is closely related and thus included here.

A multi-faceted, self-consistent model is required to make a complete evaluation of the interactions just described involving core plasma, edge plasma and liquid walls. We have made substantial progress in developing components of this comprehensive model and in using these components for initial evaluation of some of the critical issues. The status of this work is described in subsequent sections. The validation of the various computational models with experimental data is mentioned in each section. In Sec. 12.2, we give a description of the properties of the hydrogenic edge plasma obtained from the 2-D UEDGE transport code [2,3] which includes particle, momentum, and energy balance equations with variations in the poloidal and radial directions; the whole scrape-off layer plasma is typically simulated. Calculations for the ionization of the vapor as it evolves from the first wall surrounding the core-plasma and the subsequent transport of impurity ions are given in Sec. 12.3; again, the UEDGE code is used. Detailed analysis of the region near the divertor plate where magnetic field lines strike the surface at a shallow angle is presented in Sec. 12.4. Here, the WBC [4] and BPHI [5] Monte Carlo codes that follow ions and neutrals sputtered or recycled from the plate are the primary modeling tools, with some additional modeling with UEDGE. Kinetic effects for impurity transport throughout the scrape-off layer (SOL) can be studied by the MCI Monte Carlo code [6]. All of these test-particle-based codes can solve for variations in the 2-D poloidal plane, and work has begun on a 3-D version of the BPHI code. The effect of transient heat loads from ELMs and disruptions is presented in Sec. 12.5 using several codes which make up

the HEIGHTS package. Section 12.6 discusses models that will be used to assess the impact of the different edge conditions on overall performance of a fusion reactor using the ONETWO core transport code [7] which allows for radial variations of plasma parameters. Work toward direct verification of models by comparing with experiments using liquid materials is described in Sec. 12.7.

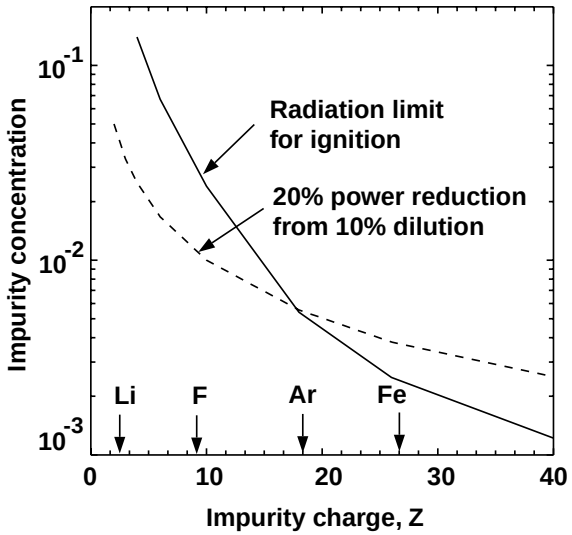

Fig. 12.1- 1 Core impurity concentration limits for different impurities due to radiation loss in a tokamak [1] and due to simple fuel dilution (dashed line).

References for Section 12.1

1. H.P. Summers, M. v. Hellermann, in: *Atomic and Plasma-Material Interaction Processes in Controlled Thermonuclear Fusion*, R. Janev, H. Darwin, eds. (Elsevier, Amsterdam, 1993) pp. 87-118.
2. T.D. Rognlien, J.L. Milovich, M.E. Rensink, and G.D. Porter, J. Nucl. Mater. **196-198**, 347 (1992).
3. T.D. Rognlien, B.J. Braams, and D.A. Knoll, Contrib. Plasmas Phys. **36**, 105 (1996).
4. J.N. Brooks, Phys. Fluids **B2**, 1858 (1990).
5. T.Q. Hua and J.N. Brooks, Phys. Plasmas **11**, 3607 (1994).
6. T.E. Evans, D.F. Finkenthal, M.E. Fenstermacher, *et al.*, J. Nucl. Mater. **266-269**, 1034 (1999).
7. H. St. John, T.S. Taylor, Y.R. Lin-lui, and A.D. Turnbull, Proc. 15th IAEA Conf., 26 Sept.-1Oct. 1994, Seville, Spain, IAEA-CN-60/D-P22, p. 603.

12.2 Edge Profiles of the Hydrogenic Plasma

We have used the 2D UEDGE code to obtain profiles of hydrogen ion density, parallel ion velocity, and separate ion and electron temperatures. The base-case is a reactor-sized tokamak (using an existing full-size ITER magnetic equilibrium) which we

term the standard-reactor case throughout this chapter. The transport simulation sets boundary conditions of power and density a small distance inside the magnetic separatrix and calculates the resulting scrape-off layer (SOL) profiles. Typically the calculations are performed for the outer half of the edge regime with reflecting boundary conditions applied at the top of the device and only the outer divertor plate included. These profiles are then used in other calculations such as the BPHI near-plate Monte Carlo code of Brooks [Sec. 12.4] and the system code studies of Evans and Wong [Sec. 12.6]. The UEDGE model for hydrogen/electron transport in the edge plasma for the high-recycling regime has been validated with data from DIII-D [1] and Alcator C-MOD [2] tokamaks.

Of particular interest has been the effect of low-recycling divertor plates such as those of liquid lithium. These calculations show that the peak heat flux actually drops in the low recycling regime because electron heat transfer is in the sheath-limited regime where there is only a small decrease in T_e between the midplane and the divertor plate. Plate electron temperature is about 220 eV for the anomalous radial transport coefficient of $D = D_0 = 0.33$ m^2/s for density and $\chi_{e,i} = \chi_0 = 0.5$ m^2/s for electron and ion energy, similar to of values used for previous ITER modeling [3,4]. In comparison, if Bohm diffusion coefficients ($=T_e/16eB$) are used, the midplane and plate electron temperature drops to 60 eV which is comparable to results obtained for diffusion coefficients of ~1.5 m^2/s. Hydrogen plasma parameters at the outer divertor plate for various parameters are shown in Table 12.2-1.

Table 12.2-1a,b Hydrogen plasma parameters at the outer divertor plate for low-recycling (R=0.5)

UEDGE simulations for (a), various anomalous diffusion coefficients, and (b), various levels of core power into the outer 1/2 of the SOL. Because of larger volume in the outer SOL region, the corresponding power into the total SOL is a factor of 1.5 larger. Here P_p is the peak poloidal heat flux, $T_{e,p}$ is peak electron temperature, and $n_{e,p}$ is the peak electron density.

a)

Anom. D and χ	P_P (MW/m^2)	$T_{e,p}$ (eV)	$n_{e,p}$ (10^{19} m^{-3})
0.5 D_0, 0.5 χ_0	49	395	0.73
D_0, χ_0	43	219	1.4
2 D_0, 2 χ_0	33	112	2.4
both $T_e/(16eB)$	25	62	3.7

b)

Power from core into outer SOL (MW)	P_p (MW/m^2)	$T_{e,p}$ (eV)	$n_{e,p}$ (10^{19} m^{-3})
100	43	219	1.4
150	57	363	0.88
200	72	516	0.62

For low recycling, there is a large particle flux out of the core that must be maintained by an edge particle-fueling source such as pellets. Such a source will have a important impact on fuel handling, burn-up fraction, and vacuum pumping. In this regime, the edge density will be controlled by this source; our base-case uses an edge density of 4×10^{19} m^{-3} which requires a large particle source of 5×10^{23} particles/s in the edge. The implementation of such a source must be included in a self-consistent modeling coupling the core performance with the edge model.

References for Section 12.2

1. G.D. Porter, *et al.*, Phys. Plasmas **3**, 1967 (1997).
2. F. Wising, *et al.*, J. Nucl. Mater. **241-243**, 273 (1997).
3. A. Kukushkin, H.D. Pacher, *et al.*, J. Nucl. Mater. **241-243**, 268 (1997).
4. M.E. Rensink and T.D. Rognlien, "Simulations for the ITER Divertor Plasma," LLNL Report no. UCRL-ID-129495, Jan. 30., 1998.

12.3 Impurities from First-Wall Evaporation

The UEDGE calculations of the hydrogen edge-plasma is augmented by including a source of impurities from the first wall (sometimes called the side wall here). There are a number of processes included in the modeling. The impurity gas is emitted from the wall in the form of atoms at typically ~1 eV if they arise from dissociation of molecules (*i.e.*, Frank-Condon-like neutrals), although a range of energies have been considered since molecular dissociation is not yet modeled in any detail, and for lithium walls, the vapor likely comes off the wall in the form of atoms. These neutrals diffuse by elastic collisions with ions until they are ionized by the electrons of the edge plasma. Once an ion, the impurity diffuses across the magnetic field with anomalous diffusion coefficients estimated from present experimental devices. Thus, the ions can diffuse radially into the core or back to the liquid wall where they are assumed to be absorbed. In addition, the ions can flow along the magnetic field and out of the system. The electron energy lost by ionizing the impurities through all of their charge states is included, so that the impinging impurities decrease the electron temperature, especially near the liquid surface. More details of the UEDGE impurity model is given in Ref. 1, and validation of the model with experimental data from the DIII-D tokamak is given in Ref. 2.

We have spent much of our effort so far this year modeling fluorine coming from a Flibe side wall, but have recently begun calculations from lithium from a SnLi side wall. Because a number of parameters in the simulation are uncertain, we have considered a range of diffusion coefficients, liquid wall boundary conditions, wall positions, impurity atomic gas temperature, and magnetic connection length (i.e., the distance out of the system along the magnetic field line). Of these, the atomic gas temperature showed the largest effect when considering the range of 0.1 eV to 10 eV; the most probably value is expected to be in the 1 eV range for Flibe. Here the core impurity level scales roughly as the thermal velocity of the gas, and thus the square root of the gas temperature. Doubling

the radial wall distance from the separatrix only decreases the impurity density by less than 50%. A three-fold reduction in the connection length reduces the impurity density by about 30%, in part because the beneficial effect of the more rapid loss out of the system is partially offset by the decrease in the hydrogen plasma-edge thickness.

Flibe is composed of the molecules BeF_2 and LiF. We focus on F because BeF_2 is much more volatile than LiF [3] and because fluorine with Z=9 radiates much more strongly than beryllium with Z=4. Consequently, the acceptable level of fluorine in the core will be smaller than beryllium (or lithium). The allowable value of the impurity edge concentration is given by $(n_{imp}/n_e)\_edge = R_{ce} <n_{imp}/n_e>\_core\_max$, where R_{ce} is the ratio of the volume-averaged core density to the edge density; we typically assume a value of $R_{ce} = 2$. From Fig. 12.1-1, we find for F that $<n_{imp}/n_e>\_core\_max = 1\%$ owing to fuel dilution. For the base-case hydrogen plasma whose divertor plate parameters are given in Table 12.2-1 (see $D=D_0$ case), the core-edge density is 4×10^{19} m^{-3} and the electron temperature is 310 eV. A typical profile of the fluorine charge states at the outer midplane of the standard-reactor tokamak is shown in Fig. 12.3-1 together with the fluorine gas density for a gas flux of 8×10^{18} $m^{-2}s^{-1}$ for the outer SOL only; fluxes should be multiplied by 1.5 to account for the full SOL, including inner and outer divertors. The surface area of the full SOL in contact with the liquid wall for this case is 1.4×10^{3} m^2. Note that charge-state 7 has the largest density at the core boundary, 2×10^{16} m^{-3} for this case, and that we omitted charge-state 9 since it is very small for these edge temperatures. Here the fluorine gas temperature is taken to be 1 eV.

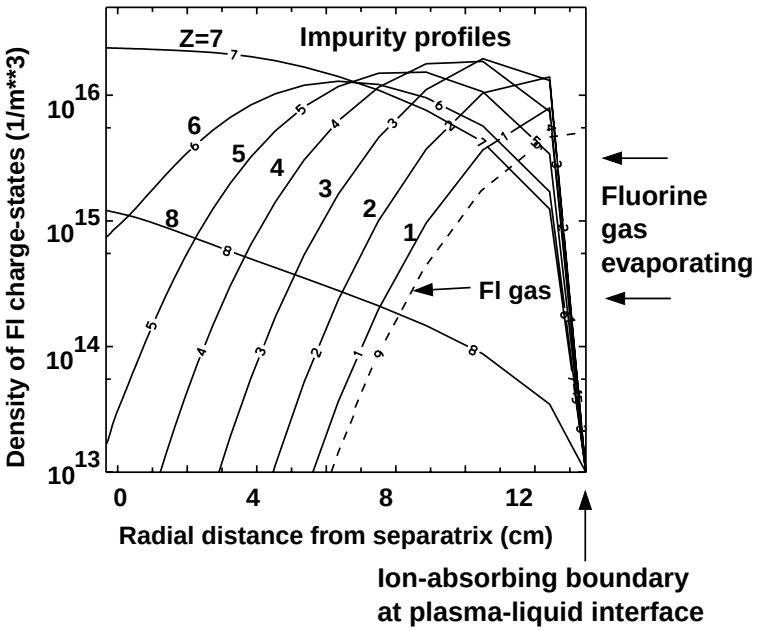

Fig. 12.3-1 Density of fluorine charge-states at the outer midplane for a gas wall flux of 8×10^{18} $m^{-2}s^{-1}$ in the reactor-size geometry

Taking a variety of simulations of the type shown in Fig. 12.3-1, we scale the fluorine gas flux until the core-edge density reaches ~2%; this corresponds to a fluorine flux of $(4\times10^{19}/2\times10^{16})\times8\times10^{18}\times0.02 \sim 3\times10^{20}$ $m^{-2}s^{-1}$. The 2% value comes from Fig. 12.1-1 where the curve giving a 20% reduction in fusion power from dilution is used together with a 2:1 density ratio between the volume-averaged core density and the core-edge density (R_{ce} = 2); the core-edge hydrogen density is 4×10^{19} m^{-3}. This F flux occurs over an area of 800 m^2 for the outer SOL, giving a current of ~4e4 Amps of F. It is assumed that the BeF_2 molecule dissociates and that the resulting two F atoms are ionized before being lost to the liquid surface; thus, the BeF_2 flux is $\sim1.5\times10^{20}$ $m^{-2}s^{-1}$. There are still a number of uncertainties in this result. In particular, if the gas temperature is closer to 0.1 eV, and a significant fraction of the dissociated atoms return to the surface before being ionized, the allowable flux of F could rise to 5×10^{20} $m^{-2}s^{-1}$, or 2.5×10^{20} $m^{-2}s^{-1}$ for BeF_2. From a curve for the evaporation rate of BeF_2 in Ref. 3, this corresponds to a surface temperature of ~540 C. Also, we do not yet model the dissociation process nor the possible recycling of F ions returning to the liquid surface (they are now assumed fully absorbed). The magnitudes of the turbulent diffusion coefficients are not well known. Furthermore, when we attempt to perform the simulation up to the full ~2% impurity level, we have not yet found a steady-state solution. It appears that an impurity MARFE (localized edge radiation zone first identified on the ALCATOR tokamak) is forming near the liquid surface which prevents steady-state solutions; more work is needed to understand this effect since the radiated power from a non-coronal equilibrium MARFE exceeds the power available from the core. Better mesh resolution is being developed near the liquid surface which could lower the impurity level by more rapid loss back to the liquid wall; the mesh resolution at the core boundary seems to be adequate.

We have just begun similar calculations for SnLi walls where only Li is evolved from the surface; it is assumed that evaporation of Sn is negligible. Here the results for impurity penetration are encouraging. Because the Li has only 3 electrons, it radiates much less than F with 9 electrons. Also, neutral Li has an ionization potential of 5.4 V compared to 17.3 V for F. Thus, Li becomes ionized sooner and has more difficulty penetrating to the core before being lost axially along the magnetic field line. Additionally, the Li gas temperature should be lower than for F since there is no appreciable role of dissociating molecules in the creation of Li atoms; the Li evaporates directly in the atomic form. As a result, a larger Li gas flux is required from the wall to obtain the same core impurity density compared to F. A case for Li is shown in Fig. 12.3-2 with a gas flux of 2×10^{20} $m^{-2}s^{-1}$ which yields an edge Li^{+3} density of 3×10^{16} m^{-3} or 0.075%; a F gas flux of 8×10^{18} $m^{-2}s^{-1}$ gives approximately the same core-edge impurity density. Scaling to an allowable edge density of Li from core fuel dilution of about 6% (again with a 2:1 density peaking factor and an edge density of 4×10^{19} m^{-3}) means that a flux of $\sim2\times10^{22}$ $m^{-2}s^{-1}$ may be permissible (see the discussion following Fig. 12.3-2). In addition, the evaporation rate of SnLi is several orders of magnitude less than Flibe, so considerably higher liquid temperatures can be tolerated; a flux of 2×10^{22} $m^{-2}s^{-1}$ corresponds to a SnLi (80%/20%) temperature of 740 C. Note that these numbers will change for difference core densities and density peaking factors.

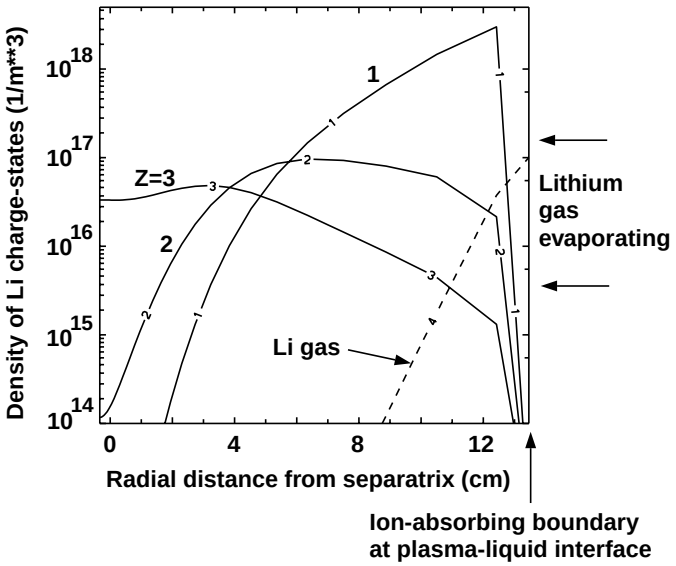

Fig. 12.3-2 Density of lithium charge-states at the outer midplane for a gas wall flux of 2×10^{20} $m^{-2}s^{-1}$ in the standard-reactor geometry. A fluorine flux of 8×10^{18} $m^{-2}s^{-1}$ used in Fig. 12.3-1 gives approximately the same impurity core density.

The comparison between the fluorine (Flibe) cases and the lithium (Li, SnLi) cases with respect to impurity concentration is shown in Fig. 12.3-3. This figure quantifies what core impurity density should be expected for a given gas flux. The gas flux can be related to the surface temperature by the evaporation rate plots shown elsewhere in this report.

It is very important to note that at higher gas fluxes, both the fluorine and lithium cases yield non-steady solutions with the UEDGE transport code as shown by the dotted lines in Fig. 12.3-3. These dotted lines are just extrapolations from the lower gas flux cases. The non-steady region corresponds to where the electron temperature near the surface abruptly drops below a few eV owing to impurity radiation and particle energy losses to the wall. This is a "detached" type of plasma, but here the detachment is from the side wall rather than the divertor plate. Note that the operating points of maximum allowable impurity concentration from Fig. 12.1-1 for a 20% reduction in fusion power correspond to ~1% for fluorine and ~3% lithium in the core region, where edge-to-center density peaking factors must be taken into account. Consequently, assuming a flat core density of $\sim1\times10^{20}$ m^{-3}, operating points for both F and Li are well into the extrapolation region shown in Fig. 12.3-3. It is thus essential to obtain more understanding of the solutions in this region. We are presently focusing on this problem and have implemented a better mesh refinement near the liquid wall to help resolve the rapid electron temperature decay.

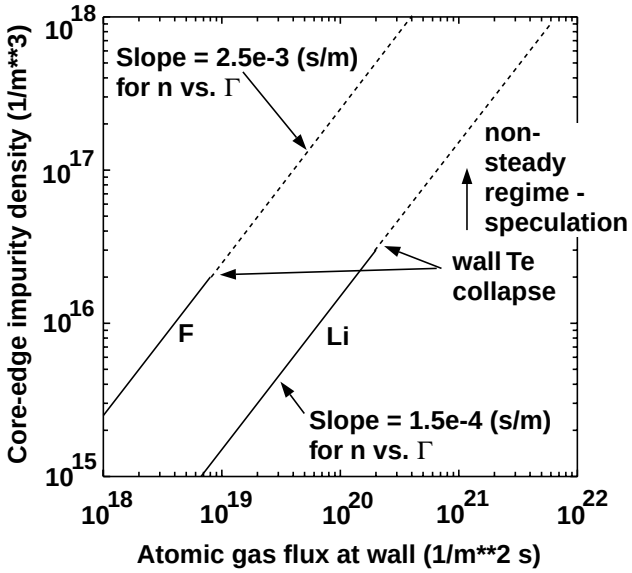

Fig. 12.3-3 Comparison of fluorine and lithium densities at the core boundary for different gas fluxes at the first wall. The dotted lines are extrapolations owing to non-steady solutions which arise with a collapse of the electron temperature just in front of the wall for larger gas fluxes.

References for Section 12.3

1. T.D. Rognlien, B.J. Braams, and D.A. Knoll, Contrib. Plasmas Phys. **36**, 105 (1996).
2. R.C. Isler, *et al.*, Phys. Plasmas **6**, 1837 (1999).
3. R.W. Moir, Nucl. Fusion **37**, 557 (1997).

12.4 Impurities from Divertor Sputtering and Evaporation

A key issue for ALPS/APEX is compatibility of wall surface material and divertor material, one issue being whether the same material can be used for both surfaces. In part for this reason a Flibe divertor surface was analyzed, along with a lithium surface. For both materials, an initial sputtering erosion/redeposition analysis was performed using the WBC Monte Carlo impurity transport code [1] with standard-reactor SOL/divertor geometry. The WBC code has been validated by comparison with measurements from the DIII-D tokamak [2]. Plasma conditions were a low-recycle plasma regime for lithium and a high-recycle regime for Flibe. A preliminary sputtering model was used for both materials.

A BPHI sheath code [3] analysis was also performed for a lithium surface with high lithium evaporation rates and with in-sheath ionization of evaporated lithium atoms considered.

For the WBC code lithium analysis, sputtered Li atoms were launched from the divertor surface into a spatially-uniform, near-surface plasma characterized by high

electron temperature and low electron density (from UEDGE code results with low D-T/Li recycling, i.e. high D-T absorption in the lithium, T. Rognlien, *et al*.). Particles are launched with a "cosine" type angular distribution, and random-collision-cascade energy distribution, and with a preliminary binding energy estimate of 3 eV. The 3-D particle trajectory is then computed with a full kinetic treatment, including Lorentz force motion and charge-changing and velocity-changing collisions with the plasma. A particle history terminates upon redeposition to the surface or leaving the ~20 cm near-surface region. The following is observed: (1) very high near-surface lithium redeposition rate (~100%), (2) high redeposited average energy with highly oblique (*i.e*., a small angle to the surface) Li ion impingement. Result (1) is favorable showing low potential for plasma contamination by sputtered lithium, even for the low-collisionality, low-recycle regime. Result (2) gives rise to concerns about runaway self-sputtering although preliminary estimates using initial ALPS/APEX project data show that this will probably not occur.

WBC calculations for Flibe assessed the near-surface transport of the individual sputtered Flibe constituents of F, Li, and Be. As with the lithium surface calculations, a highly preliminary sputtering model was used. Results for a high using a hydrogen plasma in the high-recycling regime (T_e = 30 eV, n_e =3x10^{20} m^{-3}) show a high redeposition fraction for each element. There is a lower potential for self-sputtering runaway due to lower redeposition energies and less oblique incidence.

BPHI sheath code analyses were performed for a low-recycle plasma divertor regime with a lithium surface. The surface is assumed to evaporate material owing to its heating. The BPHI code solves the full kinetic equations for D, T, Li ions and atoms, and Poisson's equation for electric field, for a tokamak-type oblique-incidence magnetic field. Sheath potential, heat transmission factor, sheath structure, and evaporated lithium redeposition fractions were self-consistently computed. Preliminary results, for one particular low-recycle regime, show that a majority of slow-moving, evaporated lithium atoms will be ionized in the sheath and will be returned to the surface due to strong sheath electric field acceleration. On the other hand, the sheath heat transmission factor (that factor, which multiplied by the particle flux and temperature, gives the energy loss) will increase due to reduced sheath potential resulting from the ion/electron in-sheath pair formation. The resulting increase in heat flux is of concern in terms of a runaway effect, but this may be mitigated by the transient nature of the overheating, and the fact that the lithium is flowing.

In the coming months, a self-consistent sputtering erosion/redeposition analysis of a lithium divertor surface is planned, using coupled UEDGE/WBC/VFTRIM codes (plasma SOL fluid code/Monte Carlo kinetic impurity code/vectorized fractal-TRIM sputtering code). This will better compute plasma contamination potential, tritium codeposition, and self-sputtering runaway potential. Additional Flibe analysis is planned along with tin-lithium analysis. A comprehensive analysis of sheath response to evaporating lithium, via BPHI code, is also planned.

As a prelude to more detailed coupling with the near-surface models just described, a few UEDGE simulations have been done (by Rognlien and Rensink) for transport in the whole SOL from a lithium physical-sputtering source at the plate. Here the sputtering neutrals are roughly modeled as a fluid gas at a fixed temperature. We considered two cases of whole-plate sputtering using an energy dependent physical sputtering model which gives a yield of 3-4% across the divertor plate. The first case assume the sputtered Li neutral had a low energy of only a few eV, in which case the ionized Li were quickly pushed back to the divertor plate from the hydrogen flow to the plate. The second case considered the sputtered Li neutral to have an energy of 100 eV to roughly model the long tail of the Thomson distribution expected from a sputtering source. Even then, the lithium density was strongly reduced by drag with the hydrogen ions, and the lithium density reaching the midplane separatrix boundary was less than 0.01%. These calculations confirm the WBC code results discussed earlier where most of the lithium is returned to the plate.

While physical sputtering of lithium from the divertor plate does not appear to be a problem, self sputtering and strong evaporation owing to heating of the surface need to be investigated in more detail. The large heat load on the divertor plate can produce a significant temperature rise even for flowing lithium which needs to be quantified in detail. Here, potentially strong lithium sources from self-sputtering and/or evaporation will substantially modify the hydrogenic edge plasma. Thus, as already mentioned, we will use the coupled WBC/UEDGE model in order to get a valid calculation for this regime.

References for Section 12.4

1.J.N. Brooks, Phys. Fluids **B2**, 1858 (1990.
2. J.N. Brooks, *et al.*, J. Nucl. Mater. **222-269**, 58 (1999); D.G. Whyte, *et al.*, J. Nucl. Mater. **222-269**, 67 (1999);
3.T.Q. Hua and J.N. Brooks, Phys.Plasmas **11**, 3607 (1994).

12.5 Effects of Large Transient Heat Loads - Disruptions

12.5.1 Plasma Interaction with Liquid Walls During Plasma Instabilities

During thermal quench phase of a tokamak plasma disruption, a sufficient part of a core plasma energy (more than 50% of total thermal energy) is delivered from the tokamak core to the scrape-off layer (SOL) and then carried to the divertor plate by energetic plasma ion and electron fluxes. Therefore, the power load to the surface is very high, reaching up to hundreds GW/m^2 over a 10^{-4}-10^{-3} s period and is capable of causing substantial damage [1]. The liquid layer protecting the structure, if removed, can result in significant heating and damage of the substrate. However, because of the developed vapor cloud at the early stages of a disruption above the divertor plate, this layer will shield the original surface from the incoming energy flux and significantly reduce the heat load onto the divertor plate surface. The dynamics of this shielding consists of the following: After the initial phase of direct heating of divertor plate surface, a vapor cloud of the divertor

surface material forms in front of the disrupting plasma and completely absorb incoming particles flux. As a result the vapor cloud is heated to temperatures of up to several tens of eV [2]. At such temperatures, the vapor plasma radiation W_{rad} becomes comparable with incoming power W_d. Because of the absorption by more cold and correspondingly more optically thick vapor plasma nearby the divertor plate surface, radiation power to the divertor plate surface is significantly decreased. HEIGHTS simulation magnetohydrodynamics (MHD) package calculations predict that radiation power W_s onto the divertor plate surface is less than 10 percents of the original incident power because of the shielding effects [3]. The main feature of this vapor shielding layer is that W_s is defined by the 'temperature of ionization' T_{ion} , below which vapor media becomes optically thin. Since this T_{ion} depends on Z, radiation power to the surface, W_s, varies from 10 MW/m^2 for heavy elements as the tungsten to about 50 MW/m^2 for light element such as beryllium and carbon-based composites. Lithium, as a candidate surface material, is the lightest condensed material and therefore special calculations were carried out using the package HEIGHTS. In this package 2-D MHD analysis of the vapor plasma is calculated using PIC methods and the radiation transport is described using the RAY Tracing method [3].

Below results are presented of plasma-material interaction calculations during a disruption for typical disruption parameters with toroidal inclination of magnetic field lines of angle $\alpha=10^o$ and poloidal angle $\phi = 30^o$, magnitude of vacuum magnetic filed $B_o = 5$ T, length of the divertor plate L=18 cm, total power of incoming plasma power flux about 700 GW/m^2, flux consists of D^+ and electrons with equal energies of 10 keV. Spatial distribution of incident power flux is taken as a Gaussian profile.

The calculations show that after an initial phase of duration $\tau_{init} \approx 20$ μs, a quasistationary state is achieved. After $t > \tau_{init}$, almost all the incoming plasma energy is transferred into photon radiation. The vapor plasma is heated to ≈20 eV at the front of expanding vapor cloud, with density $N \le 10^{18}$ cm^{-3} at the front of the expanding vapor cloud, and $N \approx 10^{19}$ cm^{-3} nearby the divertor plate surface. Density of the vapor-cloud front repeats the plasma flow shape, i.e., high density at the beam symmetry plane that decreases at the edges. Because radiation power, W_{rad}, is a quadratic function of density, the front temperature at the middle plane of the vapor cloud is less than that at the edges since the hot plasma power flow decreases from the middle to edge less than the decreasing of the radiation power. Therefore, the vapor plasma profile has a wings-like shape.

Most of the radiation power consisting of both bremsstrahlung and recombination radiation is radiated by a narrow layer at the front with high temperature of ≈ 20 eV and density of ≈ 10^{18} cm^{-3}. The line radiation of the lithium plasma has a maximum at the "ionization temperature" of ≈ 1 eV, with $Z \le 1$ nearby the divertor plate surface.

The main interest in solving this complicated problem is to predict the radiation power to the material surface, W_{in}, as the crucial factor determining divertor plate erosion.

In Fig. 12.5-1 the radiation power, W_{in}, to lithium-covered divertor plate surface is given for two different divertor geometries, i.e., normal and inclined divertor plates with poloidal angles $\varphi = 0^o$ and 30^o respectively. The "wings" structure of W_s takes place only in the case of small $\varphi \approx 0^o$ because of geometrical effects of the radiation propagation in the density profile near the target surface. It results in a more homogeneous distribution of W_{in}, but for large φ, W_{in} has a maximum that is shifted to the left, i.e., to the lower edge of divertor plate. Part of the incident electron flux with high energy and large range reaches the divertor plate surface nearby the edges because of lower density of the vapor cloud. Therefore, the total flux to divertor plate surface, $W_{total} = W_{in} + W_{ebeam}$, becomes more homogeneous. Later in time, during the course of disruption, W_{ebeam} reaching the divertor surface will be zero as the vapor cloud becomes more dense. It follows from the calculations that the radiation power to the divertor plate surface, W_{in}, is about 0.7 MW/cm^2 for $\varphi \approx 0^o$ increasing to 0.8 MW/cm^2 for $\varphi \approx 30^o$. Thus, there is a tendency of increasing radiation power to divertor plate surface with decreasing the atomic number for lighter elements. Because vapor cloud is more transparent in this case, vapor shielding is less effective and therefore more radiation energy reaches the target surface causing more splashing.

12.5.2 Erosion Mechanisms of Liquid Surfaces

Radiation power reaching the target surface will result in surface vaporization and ablation, i.e., mass losses in form of macroscopic particles. For liquid metals this ablation is in the form of droplets due to splashing of the molten layer [4]. Recent experiments to predict erosion of candidate plasma-facing components during the thermal quench phase of a tokamak plasma disruption have shown that erosion of metallic materials (such as W, Be, Al, and Cu.) can be much higher than mass losses due to surface vaporization. These mass losses are found to strongly depend on the experimental conditions such as level of incoming power, existence of a strong magnetic field, target inclination, and so on [5]. The mass losses are also found to be in the form of liquid metal droplets with sizes range from 100 A^o to tens of microns leaving the target surface with velocities U≈10 m/s. Such ablation occurs as a result of splashing of the liquid layer due to several mechanisms [6]. One main mechanism of splashing results from the hydrodynamic instabilities developed in the liquid surface (such as Kelvin-Helmholtz and Rayleigh-Taylor). Another splashing mechanism is from volume bubble boiling. These mechanisms are predicted theoretically [2] and proved experimentally [7]. It was shown that Kelvin-Helmholtz instability occurs if the vapor plasma is not well confined by the magnetic field and vapor flow takes place along the target surface. The volume bubble boiling usually takes place as a result of overheating of the liquid metal above the vaporization temperature, T_v, i.e., the temperature at which saturation pressure is equal to the outer pressure of the vapor plasma above the divertor plate surface. Therefore, the erosion energy is roughly equal to the destruction energy of splashing. The kinetic energy of the splashed droplets is calculated to be similar to that of surface tension of the liquid metal. The SPLASH code, part of the HEIGHTS package, calculates mass losses using a splashing-wave concept as a result of each erosion-causing mechanism [7]. Thus, the total erosion can be calculated from the sum of all different erosion mechanisms.

12.5.3 Droplet-Shielding Effect

A complete and accurate calculation of mass losses during plasma instabilities requires a full MHD description of vapor media nearby the target surface that consists of a mixture of vapor and droplets moving away from surface. Photon radiation energy from outermost vapor regions will then be absorbed by both the target-surface as well as the droplets cloud. This will result in the surface vaporization of both target and droplet surfaces. Therefore, in such a mixture of erosion products, further screening of the original target surface takes place due to the splashed droplets cloud. This has the effect of reducing photon radiation power to the target surface. Such screening can be called "droplets shielding" in analogy to the vapor shielding effect. Features of this droplets shielding and its influence on total mass losses is given below two cases: volume bubble boiling that has homogeneous velocities of droplets in momentum space, and the Rayleigh-Taylor instability that has droplets move normal to the surface preferentially.

The emitted macroscopic particles usually have a distribution depending on their size and velocity. We will consider, initially, particles having an average radius, R_d, and average velocity, U, in normal direction. The heat conduction from the vapor to macroscopic particles will be neglected; therefore, these particles are heated only by radiation. Due to absorption of radiation by these particles, the radiation flux, W_s, that strike the divertor plate surface will be less than the total radiation flux, W_{in}, arriving from longer distances near the hot vapor plasma toward target surface, i.e., $W_s < W_{in}$. Part of the radiation flux reaching the surface is spent for vaporization and liquid ablation, i.e., macroscopic-particle formation. As the vaporization energy per gram is much higher than the required energy for ablation, most radiation power incoming onto target surface is spent for macroscopic particle formation.

HEIGHTS package calculations show that radiation-power to the surface decreased by a factor of 5 due to droplet shielding for lithium as plasma facing material. It is also concluded that W_s does not depend on initial parameters of the macroscopic particles such as the initial radius, R_{d0}, and velocity, U, which are not well defined. This means that droplets shielding effect does not depend on size and velocity distributions of these droplets but only depends on energies of ablation destruction and vaporization; therefore, this consideration is valid for any arbitrary distribution of droplets velocities in momentum space for the studied conditions.

To summarize the simulation results, due to overheating of the divertor plate surface, macroscopic particles are splashed upstream from the surface. These particles then absorb some part of the incoming vapor radiation. The net fraction of radiation power reaching the divertor plate surface is only determined by the ratio of vaporization to splashing energies. The distance at which macroscopic-particles completely vaporize is calculated to be about 100 times the initial droplet radius. Since the initial droplet radius is small (= 10 μm), it means that droplets completely vanish at a distance L = 1 cm. Therefore, the mixture of vapor and macroscopic particles only exists very near the

divertor plate surface. Since vaporization energy is much more than splashing energy, it means that most radiation power from the upper vapor cloud is spent for vaporization. Therefore, in spite of initial large splashing-erosion the total erosion of divertor plate is defined only by vaporization losses including both divertor plate vaporization and macroscopic-particles vaporization. Again, this is only true if both the vapor-cloud and the splashed droplets are well confined in front of the disrupting plasma.

A non homogenous velocity distribution of droplets in momentum space can exists during Kelvin-Helmholtz hydrodynamic instability that arises when the vapor-plasma shear flow along the divertor surface exist as a result of MHD turbulence in the distorted oblique magnetic field lines. For this case a corresponding model is also developed that takes into account the macroscopic particles lifetime in the vapor cloud. This is implemented in the SPLASH code where the dynamics of such mixture is treated in detail simultaneously.

12.5.4 Total Mass Losses of Divertor Plate

It follows from the above discussions that vapor shielding results in a strong reduction of incoming power to the surface from incoming power of W_d =100 GW/m^2 to a power incident on the surface of W_s < 10 GW/m^2. The droplets shielding effect reduces the net power to divertor surface through droplet-vaporization. This will have the overall effect of significantly reducing the mass loss per disruption event. Such reduced value of mass losses does not appear to be excessive since the depth of liquid flow defined by heat removal requires a thickness larger than about 1 cm. It is interesting to compare this mass loss with the mass losses with and without both vapor shielding and droplet shielding as shown in Fig. 12.5-2. In case 1, i.e., in the absence of both shielding mechanisms (no vapor shielding, i.e., vapor is not well confined and no droplets shielding, i.e., droplets are splashed away from incoming plasma) all incoming energy will be spent in splash erosion of the liquid surface. In this case erosion loss is very high. This case may represent a disruption simulation device in which the incident plasma has a very high dynamic pressure. In the unrealistic case 2 without the vapor shielding but with droplet shielding, all incoming energy will be spent for vaporization of target surface. In case 3 with vapor shielding but in the absence of droplet shielding (droplets are removed away), the net incoming radiation energy to the target surface is spent for splashing. This situation can occur on nearby components during a disruption on the divertor plate where the intense photon radiation from the hot vapor cloud is deposited at these locations having different orientations to the magnetic field lines, and as a result, the vapor cloud is not well confined. This case may also represent many of the disruption simulation devices such as plasma guns and electron beams where the sample size is small and the droplets or macroscopic particles do not have enough time to absorb the incoming radiation and shield the target surface. Therefore, a well confined vapor and droplet cloud can reduce erosion losses up to two orders of magnitude.

In summary, erosion of the divertor plate as a result of shielding by both vapor and droplets clouds does not seem to be very high; therefore, divertor erosion due to the

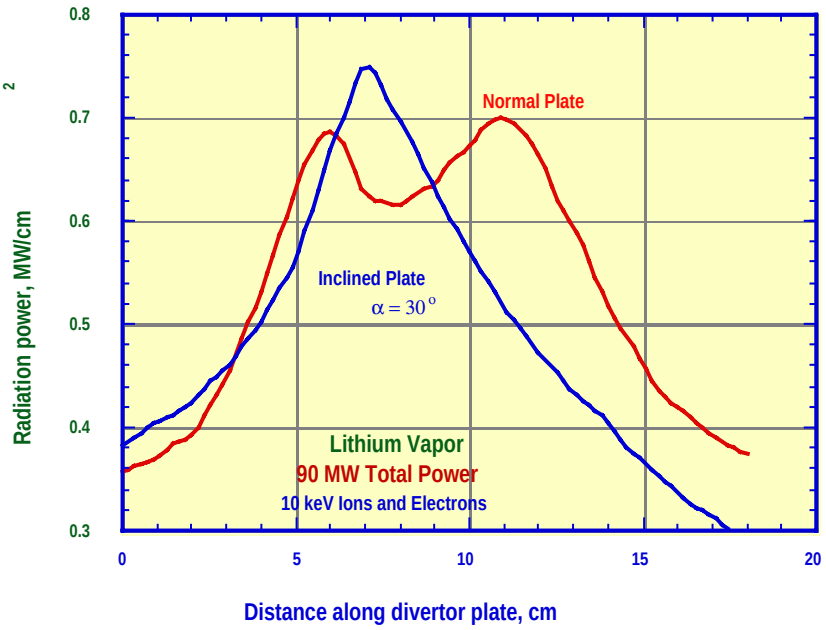

Fig. 12.5-1 Radiation power to divertor surface for normal and inclined plates.

thermal quench phase of a tokamak plasma disruption may not be the main life-limiting issue for the divertor system. Of course, this conclusion is only valid when the vapor plasma is well confined by the magnetic field vector making a small angle with the surface. However, loss of vapor confinement can occur if MHD ballooning-mode arise due to the distortion of the oblique magnetic field lines by the expanding vapor plasma [4]. In this case, turbulence results in vapor flow along the divertor plate surface. Due to this flow, first, the Kelvin-Helmholtz instability of unstable surface waves arises that results in splashing. Second, this flow blows away both vapor and droplets along the target surface. This second phenomena results in lower vapor shielding efficiency due to vapor cloud removal and, in addition, lower efficiency of droplets shielding due to the reduction of droplet exposure time in the depleted vapor.

The existence of vapor shielding that protects the divertor plates from high heat loads means that more than 90% of incoming energy is radiated to nearby locations. Therefore, the problem of erosion of other parts in a closed divertor system becomes more serious. It was shown both theoretically [8] and experimentally [9] that interaction of this 'secondary' radiation with other components results in the same consequences as the primary interaction of the SOL plasma, i.e., vapor cloud formation, splashing, and so on. Besides it may be very difficult for such vapor clouds to be well confined especially if the magnetic filed angle of inclination with different oriented surfaces is very small. Erosion of such nearby components can be estimated as in case 1, shown in Fig. 12.5-2, because of the absence of both shielding effects.

During the thermal phase of a tokamak plasma disruption, the redeposition of the eroded liquid surfaces due to vaporization and splashing will take place. As a result, all inner surfaces of the divertor system may be covered by a layer of the liquid metal surface that is condensed from vapor atoms and resolidified liquid droplets. Therefore, it is a good idea to manufacture or cover all vapor-facing materials from the same liquid that is used for the divertor surface.

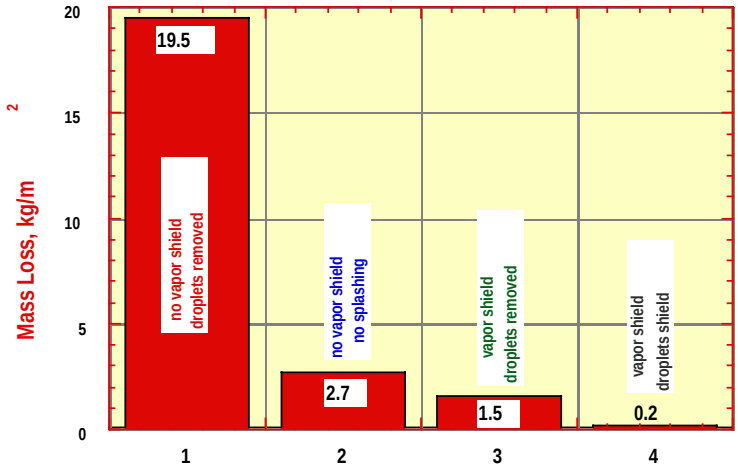

Fig. 12.5-2 Mass loss of liquid lithium due to various conditions and mechanisms.

References for Section 12.5

1. A. Hassanein, Fusion Technol. **30**, 713 (1996).
2. A. Hassanein and I. Konkashbaev, Suppl. J. Nucl. Fusion **5**, 193 (1994).
3. A. Hassanein and I. Konkashbaev, J. Nucl. Mater., in press (1999)
4. A. Hassanein and I. Konkashbaev, Plasma Devices and Operations **5**, (1998)
5. A. Hassanein and I. Konkashbaev, J. Nucl. Mater. **233-237,** 713 (1996).
6. A. Hassanein, Fusion Technol. **15**, 513 (1989).
7. A. Hassanein, G. Federici, et al., Fusion Eng. & Design **39-40**, 201 (1998).
8. A. Hassanein and I. Konkashbaev, Fusion Technol., C. Varandas and F. Serra (editors), 379 (1996).
9. V. Safronov, N. Arkhipov, et al., Fusion Technol., B. Beaumont, P. Libeyre, B. de Gentile, G. Tonon (editors), 105 (1998).

12.6 Impact of Edge Conditions on Core Performance

The goal of this task is to assess the impact of liquid divertors and first walls on the fusion power performance and cost of electricity (COE) in an ARIES-RS type reactor design. In this study, a reactor systems code is used to calculate the plasma reactivity given a set of core plasma profiles from the ONETWO transport code [1]. The systems code is used to compare reactor performance levels and subsequent COE differentials for varying core density and temperature profiles, and for different liquid materials. It is also used to estimate potential changes in current drive efficiencies and the effects of current profile control on the overall performance of the reactor.

A fundamental assumption used in this study is that the core transport physics is unaltered by changes in the boundary and scrape-off layer plasma or by the presence of the liquid wall impurities in the core plasma. This assumption may be reasonable as long as the core profile is not significantly altered by the liquid wall impurities or the properties of the ELMs are not dramatically different with liquid walls. Nevertheless, this is an issue that should be examined in future studies since changes in the core transport could have a substantial impact on the wall loading and impurity source/transport physics.

The ONETWO transport code has been extensively benchmarked on DIII-D plasmas under a wide range of operating and boundary conditions. For these studies we use ONETWO in a 1 1/2 dimensional transport mode where the initial density and temperature profiles are specified on a 1-D grid from $\rho = r/a = 0$ to $\rho = 1$ (the outer mid-plane separatrix position). The initial profiles evolve in time based on the transport model used, its associated transport coefficients, the heating profiles, and the $\rho = 1$ boundary conditions specified. The $\rho = 0$ boundary conditions, *i.e.*, $\partial X_j/\partial\rho = 0$ where $X_j = T_i$, T_e, n_i, n_e for $j = 1, 2, 3, 4$ are maintained throughout the evolution of the profiles. The $\rho = 1$ boundary conditions are established using results from the UEDGE code for cases with carbon divertor target plates, referred to here as the reference case, and for cases with liquid divertor target plates referred to as the low recycling cases.

We start with a previously established standard-reactor reference case (ITER-like) in order to determine how the transport model needs to be scaled from standard-reactor

shape in a DIII-D plasma to a reactor-sized plasma. When the standard-reactor shape is used in DIII-D a simple linear transport model, in which the ions are roughly neoclassical, is adequate to reproduce the measured core X_j profiles. The model results in relatively good power balance across the entire core with a 2.1 T, 1.6 MA DIII-D plasma. In this case the electron thermal diffusivity increases monotonically from $\chi_e(\rho = 0) \approx 0.45$ m^2/s to $\chi_e(\rho = 1) \approx 4.0$ m^2/s while χ_i peaks at approximately 0.4 m^2/s near $\rho = 0.06$ and drops to about 0.1 m^2/s at $\rho = 0.4$ then increases slowly to about 0.25 m^2/s at $\rho = 1.0$ for the initial time step. The global particle confinement time is specified to be 0.5 seconds at t = 0. For the full scale standard-reactor cases, we used the same equilibrium file as in the UEDGE simulation but converted it from a grid resolution of 65×129 to a 65×65 g0 file format. This had to be done in order to make the equilibrium file compatible with the ONETWO and the Monte Carlo Impurity (MCI) transport code [2] which is being used to assess kinetic and geometric effects on impurity transport in the scrape-off layer of the plasma.

The full-scale standard-reactor cases have $I_p = 25$ MA and $B_T = 6.05$ T with a plasma volume of 2096 m^3. For the reference case, UEDGE simulations resulted in the following $\rho = 1.0$ boundary conditions: $n_e = n_i = 4.7 \times 10^{19}$ m^{-3}, $T_e = 220$ eV, $T_i = 400$ eV, $L_{ne} = L_{ni} = 0.29$ m, $L_{Te} = 0.01$ m, and $L_{Ti} = 0.025$ m where L_{Xj} is the characteristic gradient scale-length of X_j i.e., $L_{Xj} = X_j(\partial X_j/\partial r)^{-1}$. For the low recycling case, UEDGE gave the $\rho = 1.0$ boundary conditions as: $n_e = n_i = 3.5 \times 10^{19}$ m^{-3}, $T_e = 260$ eV, $T_i = 310$ eV, $L_{ne} = L_{ni} = 0.025$ m, $L_{Te} = 0.017$ m, and both $L_{Ti} = 0.062$ m and τ_p-core had to be adjusted in order to account for a total particle loss rate of 4.5×10^{23} particles/s.

Initial ONETWO simulation of the standard-reactor reference case using the scaled up transport coefficients from DIII-D have resulted in central ion temperatures which are much larger than those specified for the ignition design point. We are in the process of scaling our χ_i profile estimates in order to establish a 20 keV central ion temperature with reasonable edge temperature and density gradients. Preliminary low recycling cases have resulted in only modest electron density changes due to small increases in the carbon impurity ion content. We have also had to use a modest amount of fast wave current drive (2.5 kA/m^2) peaked near $\rho = 0.5$ to control the bootstrap current and establish reasonable j_r profiles across the outer half of the plasma. In these plasmas the global energy confinement time reaches about 5.5 s about half way through the simulation and slowly decays until the end of the simulation. After we finish the comparison on the standard-reactor design, we will then focus on the ARIES-RS design with various liquid surface materials.

References for Section 12.6

1. H. St. John, T.S. Taylor, Y.R. Lin-lui, and A.D. Turnbull, Proc. 15th IAEA Conf., 26 Sept.-1Oct. 1994, Seville, Spain, IAEA-CN-60/D-P22, p. 603.
2. T.E. Evans, D.F. Finkenthal, M.E. Fenstermacher, *et al.*, J. Nucl. Mater. **266-269**, 1034 (1999).

12.7 Modeling Experimental Test Facilities

Experimental test facilities such as PISCES and DIII-D provide valuable data with which to benchmark codes for modeling liquid walls in reactors. Basic questions related to differences in sputtering rates and impurity transport physics with various types of liquid wall materials and plasma conditions are being addressed in the PISCES facility where we have good access to the plasma and sputtering surfaces, exceptional experimental flexibility, and excellent diagnostic coverage. Since experimental time on the DIII-D device is always in high demand, we use this facility exclusively for resolving critical issues related tokamak divertor and scrape-off layer transport issues. With its extensive array of divertor and core diagnostics, the DIII-D device gives us an opportunity to acquire a unique set of data needed to better understand how liquid wall materials may affect fusion reactor operations and performance levels.

Our approach is to use the PISCES data to validate as many of the basic physics assumptions used in our Monte Carlo Impurity (MCI) transport code as possible. Key issues such as the relative importance of chemical versus physical sputtering with various liquid wall materials and the significance of kinetic and/or molecular transport effects are currently being emphasized in these studies. An initial set of MCI simulations, characterizing the penetration of CD molecules from a CD_4 gas puff into T_i = 2.5 eV PISCES plasmas, have improved our understanding of the role molecular neutral versus ion transport and molecular gyro-radius effects as a function of the background plasma density. We are also in the process of developing more advanced reflection models that can accurately describe the interaction of various molecular species with solid and liquid surfaces in the PISCES device. The next step is to benchmark MCI's chemical and physical sputtering models against PISCES carbon target data and then against solid and liquid lithium sample exposures.

The planning for our first exposure of a liquid lithium sample to a DIII-D divertor plasma has been completed. Data from this exposure will give us information on how lithium sputtering rates and lithium impurity transport behave in a standard high recycling tokamak divertor plasma and will provide initial benchmarks for our fluid and Monte Carlo codes. The task of modeling lithium sample exposures in the DIII-D divertor involves using several specialized codes. A fluid code is used to produce the background plasma solution assuming trace lithium levels. ORNL is responsible for providing the background fluid solution using either the B2 or the UEDGE code. The ORNL fluid solution is given to ANL for near surface (< 5 cm from the sample surface) sputtering and Monte Carlo simulation using the WBC and REDEP codes. Lithium charge state densities and velocities are then passed from the ANL codes to GA's MCI code for divertor and scrape-off layer transport studies. The goal is to use measured lithium line emissions from the DIII-D experiment to benchmark these simulations. Once satisfactory benchmarks

have been achieved for high recycling DIII-D cases the codes will be used in a predictive mode to simulate the effects low recycling divertor plasmas on impurity production and transport in standard-reactor and ARIES-RS (see Sec. 12.6).

Another activity of modeling possible near-term experiments has been some initial estimates of the SOL plasma properties for the lower-single null divertor geometry in the CDX-U spherical tokamak at PPPL, for both a carbon and a lithium impurity. This modeling was done with Borass' model [1] of the SOL and divertor plasma. This model has been benchmarked to DIII-D discharges [2] by ORNL staff and has been used previously to predict [3] NSTX boundary parameters. One of the inputs to the model is the impurity species and concentration. Two simulations were done: with 5% carbon (Fig. 12.7-1) and 5% lithium (Fig. 12.7-2), to examine the impact of a dominant lithium impurity on the edge power balance. The peak heat flux with either impurity is predicted to be about 5-10 MW/m^2. This heat flux will be used to determine the plasma heating of the lithium and the subsequent lithium thermal response.

In the high divertor-temperature regime (i.e. low density/recycling), the power transmitted through the sheath dominates the hydrogen recycling and impurity line radiation sinks (Figs. 12.7-1,2). This sheath power is comparable for both carbon and lithium impurities. Note that the line radiation loss is significantly reduced for lithium, but in both cases radiation is a small part of the power balance. Note that this term ("radiation" in Fig. 12.7-2) appears to be exactly 0 in the plot for lithium but in fact is finite. This reduced line radiation term impacts the divertor parameters more in the high recycling regime (low electron temperature) regime than in the low recycling regime; thus, differences between carbon and lithium would be more observable in that regime. The big difference is that carbon may prevent access to the low recycling regime which should be achievable with lithium.

Modeling of the boundary plasma for the limiter option for CDX-U will be examined to compare it with the divertor option. While it would be easier to install a lithium limiter in CDX-U, the plasma heating may be too high and/or the toroidal asymmetry produced may be too large.

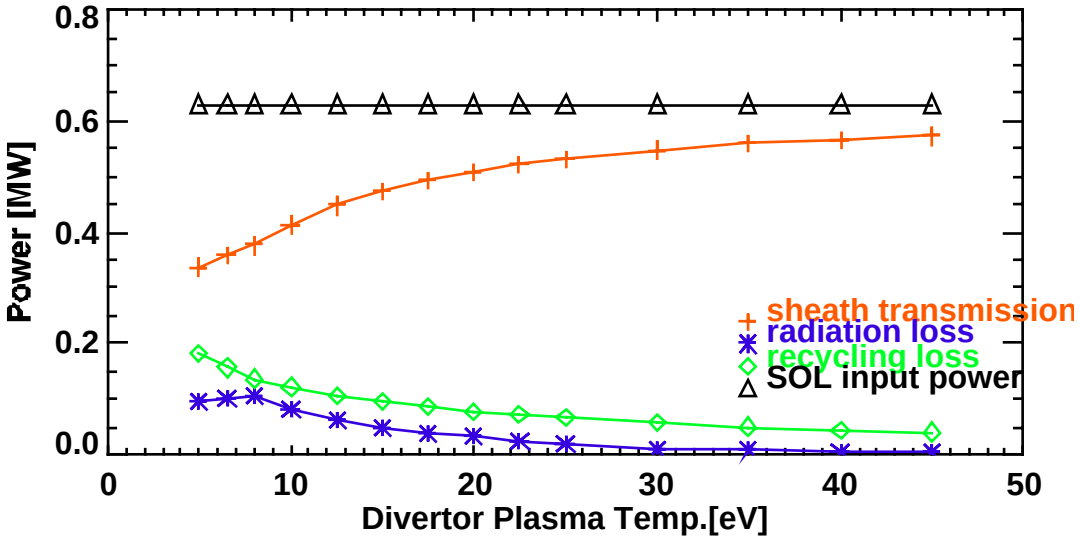

Fig. 12.7-1 Computed CDX-U edge power balance with 5% carbon impurity.

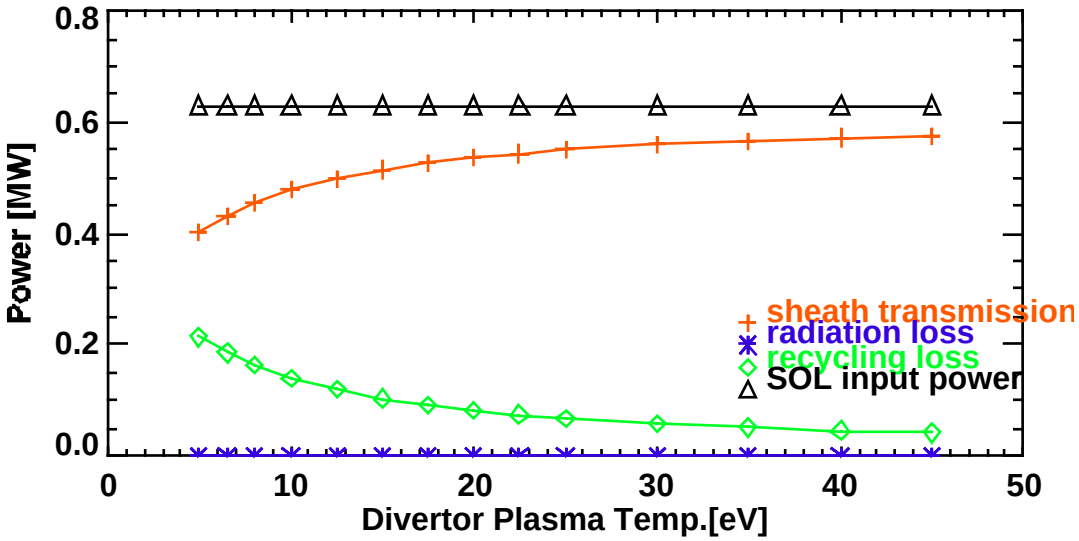

Fig. 12.7-2 Computed CDX-U edge power balance with 5% lithium impurity.

References for Section 12.7

1. K. Borass, Nucl. Fusion **31,** 1035 (1991).
2. R. Maingi, M.A. Mahdavi, T.W. Petrie, *et al.*, J. Nucl. Mater. **266-269**, 598 (1999).
3. R. Maingi, *et al*. "Estimates of Scrape-Off Layer and Divertor Parameters in NSTX", proceedings of the 1996 Workshop on the Spherical Torus, Abingdon, U.K., Dec. 4-6, 1996.